Nonlinear Response of the Cross Polar Cap Potential to Solar Wind Density Under Northward Interplanetary Magnetic Field

Ziyi Yang[1,2,3] , **Binzheng Zhang[4]** , **Jiuhou Lei[1,2,3]** , and **Tong Dang[1,2,3]**

[1]CAS Key Laboratory of Geospace Environment, School of Earth and Space Sciences, University of Science and Technology of China, Hefei, China, [2]CAS Center for Excellence in Comparative Planetology, University of Science and Technology of China, Hefei, China, [3]Mengcheng National Geophysical Observatory, University of Science and Technology of China, Hefei, China, [4]Department of Earth Sciences, The University of Hong Kong, Pokfulam, China

Abstract It is commonly believed that the magnitude and orientation of interplanetary magnetic field (IMF) together with the solar wind (SW) velocity have the most important impact on the cross polar cap potential (φ_{pc}), so that little attention has been given to the effect of SW density, especially under northward IMF conditions. Previous studies have shown that φ_{pc} increases with SW density as a response to the changes in magnetosheath force balance, while our study shows that φ_{pc} has more complicated responses to the SW density depending on the magnitude of IMF rather than a simple linear response as reported previously. The φ_{pc} may be insensitive to SW density increasing at moderate IMF B_z (cf. 8 nT) and at intense B_z (20 nT) under large-density conditions. The different behavior of SW density in regulating φ_{pc} is mainly due to the competing effects originated from viscous interaction and magnetic reconnection. Further, the physical mechanisms are explored, including the driving sources of the viscous potential and affecting factors of reconnection potential. These results pave the way for better understanding of the SW density effects on solar wind-magnetosphere-ionosphere (SW-M-I) interactions.

Plain Language Summary Ionospheric electric potential in the polar region is primarily generated due to the interaction between solar wind (SW) and magnetosphere. The cross polar cap potential (φ_{pc}), which represents difference between the maximum and minimum electric potentials in the polar cap, is closely related to the upstream interplanetary magnetic field and SW driving. SW density is one of the important dominant factors of φ_{pc}, while its physical mechanism has not been fully understood. A systematic research is conducted by using the LFM magnetosphere model to clarify the mechanism of SW density affecting φ_{pc} under purely northward interplanetary magnetic field (IMF). The simulation results demonstrate that φ_{pc} responses differently to the increasing SW density under different IMF B_z. Under small IMF B_z, φ_{pc} increases linearly with SW density, and as B_z increases, φ_{pc} becomes stable and changes little with SW density increasing. Under large IMF, φ_{pc} first increases and then becomes insensitive. These results pave the way for better understanding of the SW density effects on SW-M-I interactions.

1. Introduction

The cross polar cap potential (φ_{pc}), which represents the difference between the extrema of the electric potentials in the high-latitude ionosphere, is of critical importance in understanding the coupling between the solar wind (SW) and the magnetosphere. From the view of global-scale solar wind-magnetosphere (SW-M) coupling, φ_{pc} is driven directly by both the dayside magnetic reconnection and the viscous interaction processes between the magnetosheath and the magnetosphere (Axford & Hines, 1961; Dungey, 1961). It has been argued that the interplanetary magnetic field (IMF) or interplanetary electric field (IEF) plays the most important role in determining the value of φ_{pc} through the reconnection process during southward IMF (Axford, 1969; Burke et al., 1979; Cowley, 1973; Crooker, 1992), while other SW parameters such as the number density n are regarded as less effective in SW-M coupling. Several empirical polar cap potential models, such as the electrostatic potential determined from DMSP data and the Super Dual Auroral Radar Network (SuperDARN) system, have not considered the effect of SW density (Cousins & Shepherd, 2010; Fiori et al., 2010; Hairston et al., 1998; Ruohoniemi & Greenwald, 1996). Meanwhile, the Weimer empirical potential model for φ_{pc} is also insensitive to SW density changes (Weimer, 2005).

However, studies have shown that the SW density may have essential effects on φ_{pc}, especially under northward IMF conditions, in which case the dayside reconnection is either weaker or more localized (Heppner, 1972; Maezawa, 1976). More quantitatively, Newell et al. (2008) illustrated that functions with combined SW density and IEF exhibit better correlations for describing SW-M coupling and they incorporated SW density as a $n^{0.5}$ term in empirical SW coupling functions based on satellite data, regardless of the orientation of IMF. A similar SW density dependence has also been seen in the empirical formula for calculating φ_{pc} under zero IEF using global magnetosphere models (Bruntz et al., 2012), suggesting that φ_{pc} increases with SW density by a scaling factor of $n^{0.439}$. However, a recent study by Lin et al. (2017) investigated an event driven by large northward IMF, during which φ_{pc} changes approximately linearly with SW density n, as measured by the Resolute Incoherent Scatter Radar (Clauer et al., 2016) and reproduced in global magnetosphere simulations, suggesting that the relationship between SW density and φ_{pc} may not be simply described by the SW density alone, such as a coupling term like $n^{\sim 0.5}$ used in Newell et al. (2008).

During northward IMF driving, the inconsistency in the prediction of φ_{pc} to the changes in SW density between the coupling functions and event-based measurements is likely due to the interplay between the two physical processes that influence the dayside SW-M coupling. Previous studies have suggested two direct pathways that SW density may influence φ_{pc}: either by changing the magnetosheath force balance or by varying the viscous interaction. The former pathway affects the magnetic flux transported through the magnetosheath, which determines the reconnection potential (Lopez et al., 2010), and the latter one influences the magnitude of the viscous potential (Claudepierre et al., 2008; Eastman et al., 1976; Farrugia et al., 2001). Under northward IMF, the reconnection potential can be mapped to the ionosphere to form dusk-to-dawn electric fields across the polar cap, while the viscous potential corresponds to a dawn-to-dusk electric field at lower latitudes (e.g., Bhattarai et al., 2012; Burke et al., 1979). As SW density increases, these two electric potentials can show different variations, and the φ_{pc} depends on the interplay rather than a linear superposition of these two potentials . Thus, the response of φ_{pc} to SW density increasing is not expected to be a simple process described as a polynomial or linear term as shown in either Newell et al. (2008) or Lin et al. (2017).

Therefore, questions are still needed to be addressed in order to justify the effect of SW density on φ_{pc}: How does the φ_{pc} response to the variations of SW density under different IMF B_z? Is it linear or nonlinear? From the perspective of space weather applications, is it possible to find a parameter that better describes the dependence of φ_{pc} on SW density? In order to answer these questions, we investigate the effect of SW density on φ_{pc} under different northward IMF B_z using global models of the solar wind-magnetosphere-ionosphere (SW-M-I) system. A series of numerical simulations are conducted with similar SW/IMF inputs, except the SW density and IMF B_z. The SW density effects on potential convection patterns and their generation mechanisms under different IMF conditions are explored in detail.

2. Model Description and Settings

The LFM-MIX (the Lyon-Fedder-Mobarry and the Magnetosphere-Ionosphere Coupler/Solver) model is a three-dimensional magnetohydrodynamic (MHD) model of the coupled solar wind-magnetosphere-ionosphere system. The LFM model simulates the interactions between the SW and magnetosphere by solving ideal MHD equations on a nonorthogonal curvilinear grid adapted to magnetospheric problems using a finite-volume scheme (Lyon et al., 2004; Zhang et al., 2017). The MIX code provides a solution of ionospheric electric potential through electrostatic current closure with field-aligned current and height-integrated conductance given at ionospheric reference altitudes (Merkin & Lyon, 2010). In this simulation, the popular double resolution of the LFM model is used, which uses $53 \times 48 \times 64$ cells in the radial, meridional, and azimuthal directions, corresponding to a $2° \times 2°$ resolution in magnetic latitude (MLT) and magnetic local time (MLAT) at ionospheric reference altitude of 100 km.

A series of simulations have been performed using the SW/IMF inputs listed in Table 1. Each group has the same time-independent upstream driving conditions, except for the magnitude of IMF B_z and the SW number density. To simplify the analysis, the ionospheric Pedersen conductance is set to uniformly 5 mhos, and the Hall conductance is set to zero in order to eliminate feedback effects from ionospheric electrodynamics; ionospheric conductance affects the spatial distribution of φ_{pc} through gradients in nightside auroral conductance, which is much less important for SW density driving (Lotko et al., 2014). Three magnitudes

Table 1
The B_z Component, Solar Wind Density, and Other Settled Input Solar Wind Data for Different Simulations

SW/IMF Parameters	Values
B_z (nT)	1, 8, 20
n (cm^{-3})	4, 8, 12, 16, 20, 24
V_x (km/s)	−400
C_s (km/s)[a]	40
V_y, V_z, B_x, B_y	0

[a]The sound speed of the solar wind.

of B_z, 1, 8, and 20 nT, are used in this study to represent weak, moderate, and intense IMF driving conditions, respectively. The SW density varies from 4 to 24 cm^{-3}, which is within the range of typical observed SW densities (Lin et al., 2017; Rout et al., 2016). Each simulation is run for 10 hr driven by the specific SW/IMF conditions. The ionospheric potentials are derived from the 1-hr average data during 9–10 hr when the system is in a quasi-steady state without any isolated substorm activities.

3. Results and Discussion

Figure 1 shows the variations of φ_{pc} with SW density driven by three magnitudes of northward IMF B_z, representing weak (1 nT), moderate (8 nT), and intense (20 nT) drivings, respectively. The dynamic range of the φ_{pc} under $B_z = 1$ nT at 24 cm^{-3} is relatively larger compared to other cases, due to the viscous interaction becomes more dynamic as the SW density increases. It is shown that in the weak IMF case, φ_{pc} increases approximately linearly from 11.49 to 49.13 kV as the SW density increases from 4 to 24 cm^{-3}. Under intense IMF driving, the φ_{pc} exhibits a nonlinear response, which first increases from 52.16 to 65.06 kV as SW density increases from 4 to 12 cm^{-3} and then decreases from 64.8 to 58.7 kV as the SW density increases from 16 to 24 cm^{-3}. The increasing φ_{pc} with SW density in the intense case is generally consistent with the event studied by Lin et al. (2017), except a small decrease in φ_{pc} with further increase in the SW density. However, the moderate IMF case exhibits completely different behavior compared to the other two; that is, the φ_{pc} remains approximately insensitive around 22.0 kV regardless of the magnitude of the SW density, which is unexpected based on previous studies and cannot be described quantitatively by either the $n^{0.5}$ term used in Newell et al. (2008) or the linear relation found by Lin et al. (2017). For example, measurements from Resolute Incoherent Scatter Radar (RISR-N) during 0:00–1:37 UT on 4 August 2017 (figure not shown) have shown opposite responses of ionospheric electric field (E_{RISR-N}) with increasing SW density compared to predictions using the Lin et al. (2017) mechanism. In this moderate northward IMF B_z event ($B_z \approx 10$ nT), the E_{RISR-N} shows significant reduction from ~44 to ~27 mV/m as the SW density increases from ~22 to ~40 cm^{-3}, while other SW/IMF conditions remained approximately unchanged (with variations less than 15%). The response of E_{RISR-N} during this event is consistent with the theoretical predictions in the moderate IMF case but exhibits a negative dependence on SW density, which cannot be explained using changes in either merging or viscous interaction alone. More comprehensive data-model comparison is needed to further quantify the role of SW density on regulating the φ_{pc} especially during moderate IMF driving conditions, which will be performed in a follow-up study. The different responses of φ_{pc} to increasing SW density under different IMF conditions suggest that it may be inaccurate to simply use the parameter n as an independent function to quantify the response of φ_{pc} to increasing SW density and another physical parameter regulated by the SW density is needed.

Figure 2 shows the simulated spatial distributions of ionospheric potential in the magnetic coordinates, which compares the responses of potential patterns for the small (4 cm^{-3}) and the large (16 cm^{-3}) SW density cases. The open-close boundaries derived from the simulated average magnetic field are only shown in Figures 2c–2f, as the magnetotail under $B_z = 1$ nT driving is too long so that some magnetic field lines exceed the antisunward boundary of the LFM grid ($X_{min} \approx -300$ R$_E$), which induces uncertainties in the calculation of the open-close boundary (Farrugia et al., 2007).

Figures 2a and 2b display the simulated distributions of φ_{pc} driven by IMF $B_z = 1$ nT. Two large convection cells, as indicated by the vectors of perpendicular plasma drift, appear in the high-latitude region in
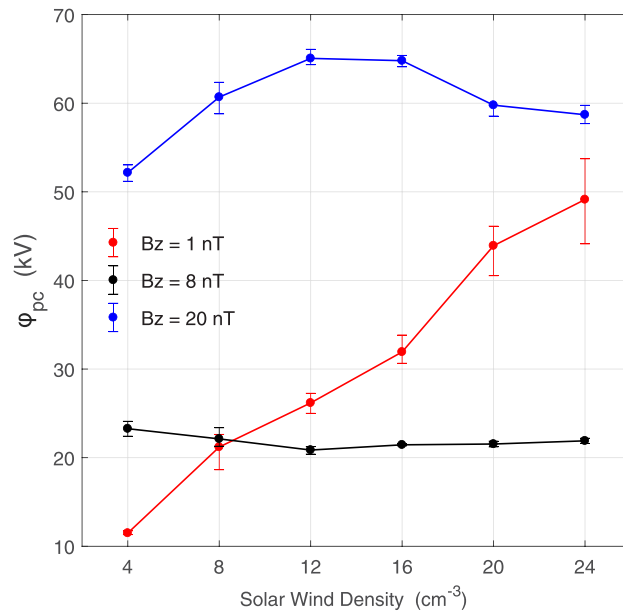
Figure 1. Variations of φ_{pc} under $B_z = 1$ nT (red), $B_z = 8$ nT (black), and $B_z = 20$ nT (blue) with SW density increasing. The error bar denotes the variations of φ_{pc} within the 10th hour of the simulation.

Figure 2a, with the potential extrema centered between ~70° N and 80° N MLAT. The positive potential cell locates on the dawnside and negative potential cell locates on the duskside, corresponding to a dawn-to-dusk polar cap electric field, which are mainly mapped along the closed magnetic field lines as shown in Figure S1 in the supporting information. Compared to Figure 2a, the potential cells shown in Figure 2b are enhanced as density increases from 4 to 16 cm^{-3}.

The corresponding spatial distributions of φ_{pc} under $B_z = 8$ nT are shown in Figures 2c and 2d, driven by SW densities of 4 and 16 cm^{-3}, respectively. Four-cell convection patterns are evident in the polar region
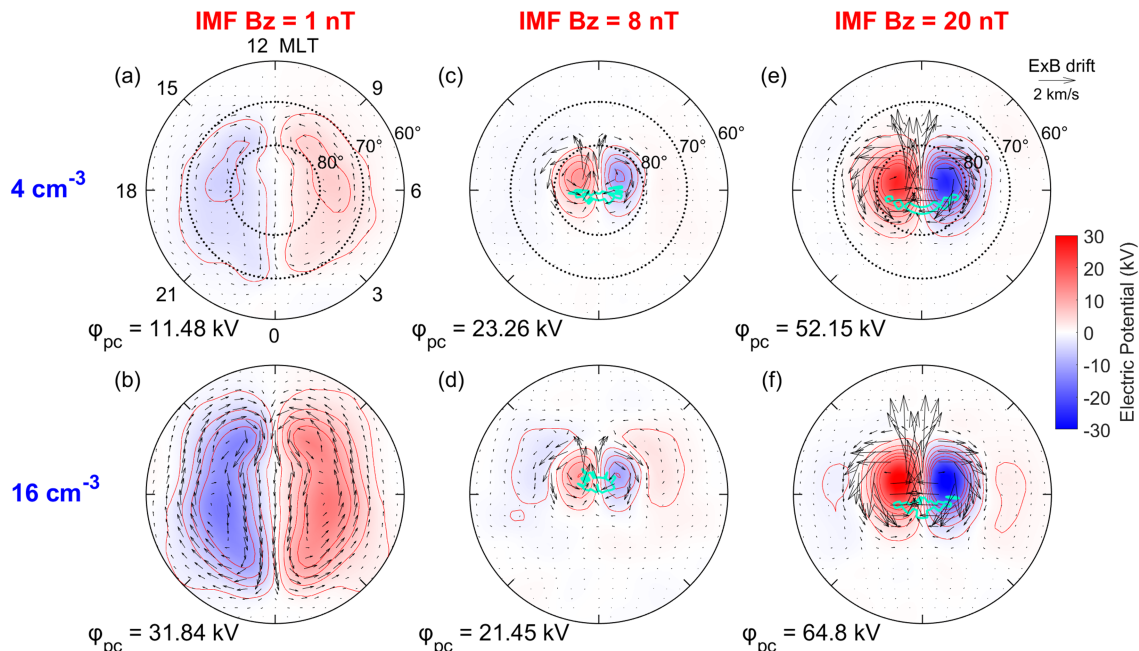

Figure 2. The simulated snapshots of electric potential (red contours), ion drift (black arrows) and open-closed boundary (cyan contour) of the Northern hemisphere in the SM coordinate. From left to right, the panels correspond to the same SW density under different northward IMF.
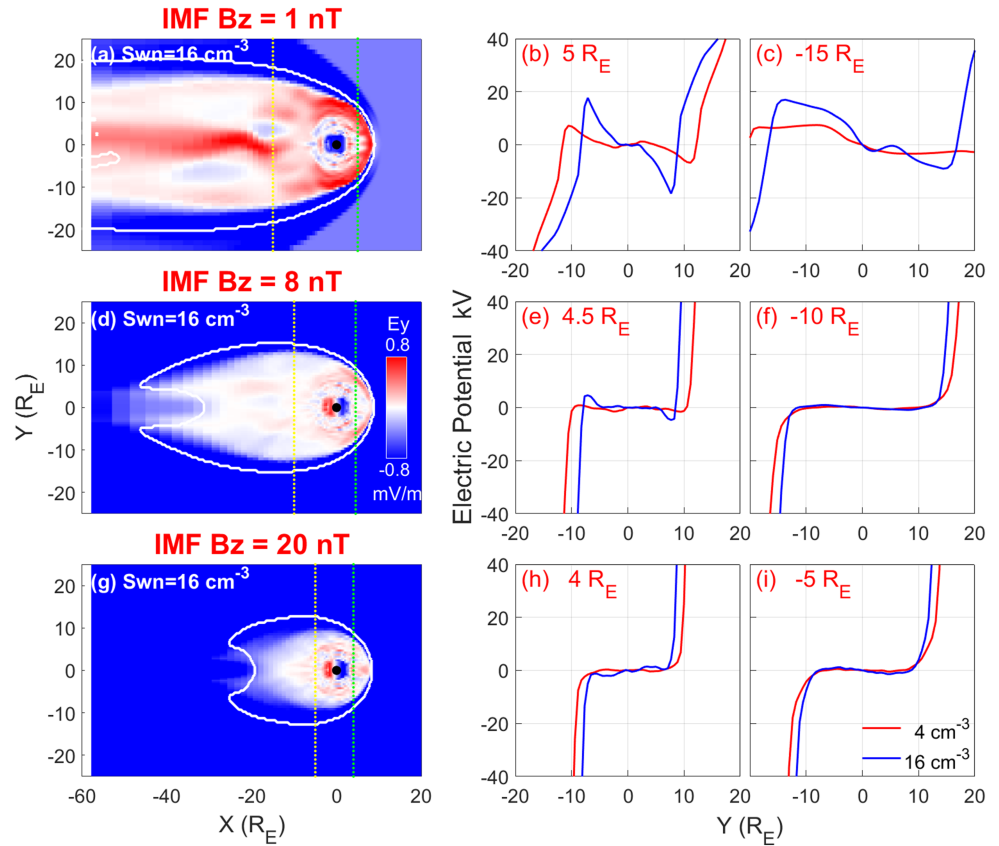
Figure 3. The snapshots about the equatorial plane (a, d, g) show the E_y component of electric field for SW density of 16 cm^{-3} under different IMF. The green and yellow lines mark out the positions of the sample lines. Figures 3b- 3c, 3e- 3f and 3h- 3i are the potentials integrated from the E_y component of electric field along the sample lines. The red (4 cm^{-3}) and blue (16 cm^{-3}) represent different magnitudes of SW densities.

in Figure 2d (e.g., Burke et al., 1979). Unlike the IMF $B_z = 1$ nT case shown in Figures 2a and 2b, φ_{pc} is dominated by merging cells located between 80° N and 90° N MLAT, associated with a dusk-to-dawn electric field driving sunward convection near the pole. The two viscous cells at lower latitudes in Figure 2d are located equatorward of the open-close boundary, indicating that they are mapped along the closed magnetic field lines. Although the viscous cells in the polar region under $B_z = 8$ nT have similar physical origins as those under $B_z = 1$ nT, they are weaker and occurred mostly on the dayside of the polar region, rather than appearing as two large cells in Figures 2a and 2b. Thus, the φ_{pc} is almost not influenced by the enhanced viscous cells in Figure 2d. Figures 2e and 2f show the electric potentials under $B_z = 20$ nT. In this case, the viscous potential cells are almost negligible, and the simulated φ_{pc} is completely dominated by the merging cells, with larger spatial extensions and greater magnitudes than those in the $B_z = 8$ nT case. The comparison suggests that the response of viscous and merging potentials to SW density is the key to quantify the response of φ_{pc}; therefore, the variations of these two kinds of potentials are discussed in detail in the following to understand the underlying mechanisms that control the response of φ_{pc} to SW density.

In a mostly closed magnetosphere driving by northward IMF, the changes in viscous potential mapped to the ionosphere are related to the variations in the convective electric field in the equatorial magnetosphere induced by viscous interactions. In this study due to the symmetry of the simulation setup, the *y* component of the electric field (E_y) in the equatorial plane has the most prominent influence on φ_{pc}, as shown in Figure 3. Thus, the corresponding viscous potential contributing to the ionospheric viscous cells is approximately estimated by integrating E_y along dawn-dusk lines (denoted by the green and yellow lines in Figures 3a, 3d, and 3g). As IMF B_z increases, although the global magnetosphere is compressed significantly, the spatial extension of the dayside magnetosphere between 9 and 15 MLT is much less influenced compared to the magnetotail, as indicated by the open-close boundary. Therefore, the dawn-dusk cut lines for estimating the intensities of viscous interaction in the magnetotail under $B_z = 1$ nT (Figure 3a), $B_z = 8$ nT
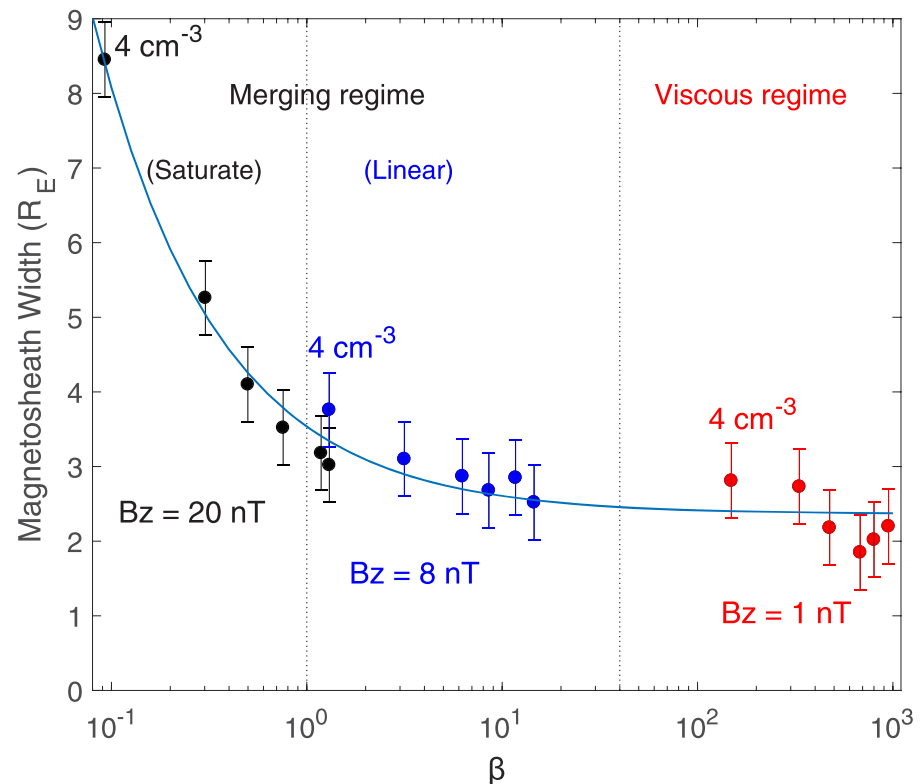
Figure 4. Variations of magnetosheath width with magnetosheath plasma β under different IMF B_z, with the solid line derived from exponential fitting, which is $1.173e^{-1.583\lg\beta} + 2.364$. The plasma β is calculated from the average value in the magnetosheath at noon-midnight meridian plane, and the magnetosheath width is calculated from the distance between the bow shock and the magnetopause at the line of $Y = 0$ R_E, $Z = 0$ R_E (SM). The error bar corresponds to 0.5 R_E, associated with the minimum resolution of the grid.

(Figure 3d), and $B_z = 20$ nT (Figure 3g) are chosen as $X = -15$ R_E, $X = -10$ R_E, and $X = -5$ R_E, respectively. On the dayside, the x locations of the dawn-dusk cut lines for estimating the dayside viscous interaction are only decreased with an interval of 0.5 R_E, locating at $X = 4$ R_E, $X = 4.5$ R_E, and $X = 5$ R_E. The E_y components along the sample lines are integrated using a numerical quadrature with the zero potential chosen at $Y = 0$ R_E.

In Figures 3b and 3c, the integrated equatorial potentials at $X = 5$ R_E and $X = -15$ R_E have substantial values with a maximum potential drop of 13.96 and 36.08 kV driven by SW density 4 and 16 cm^{-3}, respectively, which is approximately consistent with the φ_{pc} (11.8 and 31.8 kV) as shown in Figures 2a and 2b. These electric fields are mainly induced by the viscous interactions, which are strengthened as SW density increases (e.g., Bruntz et al., 2012) due to the enhancement of Kelvin-Helmholtz instability inside the flanks of the magnetopause (Claudepierre et al., 2008; Farrugia et al., 2001). Therefore, in the weak IMF case, the φ_{pc} shows a significant increase with the SW density.

Figures 3d–3f display the integrated equatorial potentials along $X = 4.5$ R_E and $X = -10$ R_E in the moderate IMF case. When driven by $B_z = 8$ nT, the y component of the equatorial convective electric field is much smaller compared to the weak B_z case, and the magnitude of the electric field near the nose of the magnetopause is greater than the magnetotail. Normally, the viscous interaction is expected to be more intense in the magnetotail (Axford & Hines, 1961; Merkin et al., 2013), while as the B_z increases, the magnetosphere is compressed significantly, which suppresses the viscous interactions along boundaries of the magnetotail (Bhattarai & Lopez, 2013). As discussed in Figure S2, the stronger electric field at the nose of the magnetopause is probably due to the stronger magnetic fields there. Thus, the viscous potential in the polar cap is more dependent on the dawn-dusk electric fields near the dayside of the magnetopause. As shown by the integrated electric field along dawn-dusk cut lines, for a moderate IMF driving, the equatorial potential

increases from 2.43 to 9.29 kV as SW density increases from 4 to 16 cm^{-3}. Since the φ_{pc} is dominated by merging potential, which is about 23.26 and 21.45 kV as shown in Figures 2c and 2d, the viscous potential is much smaller and has little effects on φ_{pc}. Similarly in the intense IMF case shown in Figures 3g–3i, the magnetosphere is further compressed with even smaller integrated dayside, viscous-induced equatorial potential (1.06 and 3.44 kV), indicating that the viscous interaction is essentially suppressed due to the reduction of velocity shear across the magnetopause (Bhattarai & Lopez, 2013). Therefore, the viscous potential is not important for φ_{pc} under large northward B_z.

The comparisons in Figures 2 and 3 indicate that both the viscous potential and merging potential may exhibit a positive response with increasing SW density. However, due to the interplay between the viscous interaction and dayside merging, these two kinds of potentials may exhibit different behaviors under different IMF conditions. Thus, incorporating the influence of SW density as a simple polynomial term ($n^{\sim 0.5}$) may be an oversimplification of the underlying physical processes, which should be at least combined with B_z as a zeroth-order correction. According to the force balance model, the change in magnetosheath plasma β is likely a good candidate to quantify the nonlinear response of φ_{pc}, since both the merging cell and viscous cell are influenced by β, which is regulated by a combination of IMF and SW density and can be written as $(v_s^2\rho/\gamma)/(B^2/2\mu_0)$, where v_s is the sonic speed and γ is the ratio of specific heat.

Figure 4 shows the relationship between the simulated magnetosheath width and the average magnetosheath β derived from all the simulations. It is evident that as β increases from 10^{-1} to 10^2 and the magnetosheath width decreases rapidly at first but then turns to decrease more gradually. This is because small magnetosheath plasma β corresponds to SW conditions with low magnetosonic Mach number (M_{MS}). In the low-β regime, the bow shock compression ratio is sensitive to variations in M_{MS} due to the transition between submagnetosonic and supermagnetosonic SW (Lavraud & Borovsky, 2008; McKean et al., 1996). Thus, a small increase in SW density causes significant compression of the bow shock (Chapman & Cairns, 2003; Lopez et al., 2004). As β gets much larger than 1, the reduction of the magnetosheath width is much less sensitive to the increasing β since it is more hydrodynamic and is dominated by the pressure gradient force rather than the Lorentz force.

Using the magnetosheath force balance model developed by Lopez et al. (2010), the pathways of SW density influence on the φ_{pc} may be explained in terms of magnetosheath β. In the $B_z = 20$ nT case, the magnetosheath is dominated by the Lorentz force as SW density increases from 4 to 12 cm^{-3} (the former part of the black points when $\beta \ll 1$), which is already in the saturate regime for IMF B_z. Together with the negligible viscous potential, the φ_{pc} is dominated by dayside merging and increases approximately linearly as SW density increases from 4 to 12 cm^{-3}, which fits the event studied by Lin et al. (2017). However, with the further increase of SW density, the magnetosheath turns to be dominated by pressure gradient fore, and the system is transitioned into the linear region for IMF. In this regime the magnetosheath condition is propitious for the SW magnetic flux to be transported, and the merging potential will increase as soon as the IMF increases (Lin et al., 2017). While in this simulation, the magnitude of the IMF B_z is constant, and it is the magnitude of the IMF rather than the SW pressure (Siscoe et al., 2002) that limits the value of φ_{pc}. Thus, although the SW density keeps increasing, the magnetic flux that can be transported through the magnetosheath is getting saturated, and this leads to the saturation of φ_{pc}. In addition, in the intense IMF case, with the evident compression of the magnetosphere, the geoeffective length of the SW also decreases as shown in Figure S3, given that the IEF was fixed (+20 nT), such a reduced reconnection separator has a negative effect on the merging potential and leads to the decrease of φ_{pc}, as shown in Figure 1 when SW density increases from 16 to 24 cm^{-3} under $B_z = 20$ nT.

For $B_z = 8$ nT, β almost locates between 1 and 10, which is also in the linear regime for IMF, and the magnetic flux that can be transported is also limited by the constant IMF, and as a result, the φ_{pc} remains unchanged. Note that under $B_z = 8$ nT, the magnetosheath width is out of the rapid-decline period as shown in Figure 4; thus, the separator is not greatly shrunken, and the φ_{pc} does not show evident decrease as SW density increases. In the $B_z = 1$ nT case, the plasma $\beta \gg 1$, and the pressure gradient force is the dominated force in magnetosheath. The magnetosheath width cannot be further compressed, resulting in little change in the merging process. As the viscous potential dominates φ_{pc} in this parameter regime, φ_{pc} goes linearly with increasing SW density.

The results in Figure 4 suggest that the response of φ_{pc} may be better regulated by the magnetosheath plasma β, rather than SW density alone. The φ_{pc} under different magnitudes of northward IMF can show

different variations with the increasing of SW density, and the variation can be roughly divided into three stages, linear-increasing regime for merging potential, insensitive (sometimes decreasing) regime for merging potential, and the linear-increasing regime for viscous potential. In the first two periods, the φ_{pc} is dominated by merging potential, and the dividing line between the two regimes locates near $\beta = 1$. In the third period, the φ_{pc} is dominated by viscous potential, and it increases evidently with SW density, which has been widely discussed. The φ_{pc} under each magnitudes of northward IMF can have these three stages, their dividing lines may locate little differently, but their variation mechanisms are the same. In this study, the φ_{pc} variations with SW density are roughly represented with the magnetosheath β; a more accurate representation of β may be studied in the further work for better application.

4. Conclusion

In this study, the effect of SW density on φ_{pc} under different northward IMF is studied based on a global model of the coupled SW-M-I system. The simulation results show that φ_{pc} displays different variations with SW density driven by different IMF magnitudes. For weak IMF ($B_z = 1$ nT), φ_{pc} increases approximately linearly due to the enhancement of the viscously-induced electric field in the equatorial magnetosphere, driven by enhanced viscous interactions. For moderate IMF, the response of φ_{pc} to increasing SW density is determined by the interplay between the viscous interaction and dayside merging. In the specific case analyzed in this study (IMF $B_z = 8$), the merging potential dominates the increase in the viscous potential, which changes little with increasing SW density due to less influenced force balance in the magnetosheath, the φ_{pc} is insensitive to the changes in SW density. For large IMF ($B_z = 20$ nT), φ_{pc} rises firstly and then gets saturated as SW density increases. Small SW density results in a small magnetosonic Mach number under large B_z, and the magnetosheath could be significantly compressed. More magnetic flux can get into the magnetosphere to reconnect with geomagnetic fields, which leads to an increase of reconnection potential and φ_{pc}. Afterwards, φ_{pc} turns to get saturated as the magnetic flux that can be transported into the magnetosphere is limited by the constant IMF B_z. Our results illustrate that the influence of SW density on φ_{pc} varies with the magnitude of B_z, even in the northward IMF conditions.

References

Axford, W. I. (1969). Magnetospheric convection. *Reviews of Geophysics*, 7(1-2), 421–459. https://doi.org/10.1029/RG007i001p00421

Axford, W. I., & Hines, C. O. (1961). A unifying theory of high-latitude geophysical phenomena and geomagnetic storms. *Canadian Journal of Physics*, 39(10), 1433–1464. https://doi.org/10.1139/p61-172

Bhattarai, S. K., & Lopez, R. E. (2013). Reduction of viscous potential for northward interplanetary magnetic field as seen in the LFM simulation. *Journal of Geophysical Research: Space Physics*, 118, 3314–3322. https://doi.org/10.1002/jgra.50368

Bhattarai, S. K., Lopez, R. E., Bruntz, R., Lyon, J. G., & Wiltberger, M. (2012). Simulation of the polar cap potential during periods with northward interplanetary magnetic field. *Journal of Geophysical Research*, 117, A04219. https://doi.org/10.1029/2011JA017143

Bruntz, R., Lopez, R. E., Wiltberger, M., & Lyon, J. G. (2012). Investigation of the viscous potential using an MHD simulation. *Journal of Geophysical Research*, 117, A03214. https://doi.org/10.1029/2011JA017022

Burke, W. J., Kelley, M. C., Sagalyn, R. C., Smiddy, M., & Lai, S. T. (1979). Polar cap electric field structures with a northward interplanetary magnetic field. *Geophysical Research Letters*, 6(1), 21–24. https://doi.org/10.1029/GL006i001p00021

Chapman, J. F., & Cairns, I. H. (2003). Three-dimensional modeling of Earth's bow shock: Shock shape as a function of Alfvén mach number. *Journal of Geophysical Research*, 108(A5), 1174. https://doi.org/10.1029/2002JA009569

Claudepierre, S. G., Elkington, S. R., & Wiltberger, M. (2008). Solar wind driving of magnetospheric ULF waves: Pulsations driven by velocity shear at the magnetopause. *Journal of Geophysical Research*, 113, A05218. https://doi.org/10.1029/2007JA012890

Clauer, C. R., Xu, Z., Maimaiti, M., Ruohoneimi, J. M., Scales, W., Hartinger, M. D., & Lopez, R. E. (2016). Investigation of a rare event where the polar ionospheric reverse convection potential does not saturate during a period of extreme northward IMF solar wind driving. *Journal of Geophysical Research: Space Physics*, 121, 5422–5435. https://doi.org/10.1002/2016JA022557

Cousins, E. D. P., & Shepherd, S. G. (2010). A dynamical model of high-latitude convection derived from superDARN plasma drift measurements. *Journal of Geophysical Research*, 115, A05218. https://doi.org/10.1029/2010JA016017

Cowley, S. W. H. (1973). A qualitative study of the reconnection between the Earth's magnetic field and an interplanetary field of arbitrary orientation. *Radio Science*, 8(11), 903–913. https://doi.org/10.1029/RS008i011p00903

Crooker, N. U. (1992). Reverse convection. *Journal of Geophysical Research*, 97(A12), 19,363–19,372. https://doi.org/10.1029/92JA01532

Dungey, J. W. (1961). Interplanetary magnetic field and the auroral zones. *Physical Review Letters*, 6(2), 47. https://doi.org/10.1103/PhysRevLett.6.47

Eastman, T. E., Hones Jr, E. W., Bame, S. J., & Asbridge, J. R. (1976). The magnetospheric boundary layer: Site of plasma, momentum and energy transfer from the magnetosheath into the magnetosphere. *Geophysical Research Letters*, 3(11), 685–688. https://doi.org/10.1029/GL003i011p00685

Farrugia, C. J., Gratton, F. T., & Torbert, R. B. (2001). Viscous-type processes in the solar wind-magnetosphere interaction. *Space Science Reviews*, 95(1-2), 443–456. https://doi.org/10.1023/A:1005288703357

Farrugia, C. J., Grocott, A., Sandholt, P. E., Cowley, S. W. H., Miyoshi, Y., Rich, F. J., & Sharma, A. (2007). The magnetosphere under weak solar wind forcing. *In Annales Geophysicae*, 25(1), 191–205. https://doi.org/10.5194/angeo-25-191-2007

Fiori, R. A. D., Boteler, D. H., Koustov, A. V., Haines, G. V., & Ruohoniemi, J. M. (2010). Spherical cap harmonic analysis of Super Dual Auroral Radar Network (SuperDARN) observations for generating maps of ionospheric convection. *Journal of Geophysical Research*, 115, A07307. https://doi.org/10.1029/2009JA015055

Hairston, M. R., Heelis, R. A., & Rich, F. J. (1998). Analysis of the ionospheric cross polar cap potential drop using DMSP data during the national space weather program study period. *Journal of Geophysical Research*, *103*(A11), 26,337–26,347. https://doi.org/10.1029/97JA03241

Heppner, J. P. (1972). Polar-cap electric field distributions related to the interplanetary magnetic field direction. *Journal of Geophysical Research*, *77*(25), 4877–4887. https://doi.org/10.1029/JA077i025p04877

Lavraud, B., & Borovsky, J. E. (2008). Altered solar wind-magnetosphere interaction at low mach numbers: Coronal mass ejections. *Journal of Geophysical Research*, *113*, A00B08. https://doi.org/10.1029/2008JA013192

Lin, D., Zhang, B., Scales, W. A., Wiltberger, M., Clauer, C. R., & Xu, Z. (2017). The role of solar wind density in cross polar cap potential saturation under northward interplanetary magnetic field. *Geophysical Research Letters*, *44*, 11,729–11,734. https://doi.org/10.1002/2017GL075275

Lopez, R. E., Bruntz, R., Mitchell, E. J., Wiltberger, M., Lyon, J. G., & Merkin, V. G. (2010). Role of magnetosheath force balance in regulating the dayside reconnection potential. *Journal of Geophysical Research*, *115*, A12216. https://doi.org/10.1029/2009JA014597

Lopez, R. E., Wiltberger, M., Hernandez, S., & Lyon, J. G. (2004). Solar wind density control of energy transfer to the magnetosphere. *Geophysical Research Letters*, *31*, L08804. https://doi.org/10.1029/2003GL018780

Lotko, W., Smith, R. H., Zhang, B., Ouellette, J. E., Brambles, O. J., & Lyon, J. G. (2014). Ionospheric control of magnetotail reconnection. *Science*, *345*(6193), 184–187. https://doi.org/10.1126/science.1252907

Lyon, J., Fedder, J., & Mobarry, C. (2004). The Lyon-Fedder-Mobarry (LFM) global MHD magnetospheric simulation code. *Journal of Atmospheric and Solar-Terrestrial Physics*, *66*(15-16), 1333–1350. https://doi.org/10.1016/j.jastp.2004.03.020

Maezawa, K. (1976). Magnetospheric convection induced by the positive and negative z components of the interplanetary magnetic field: Quantitative analysis using polar cap magnetic records. *Journal of Geophysical Research*, *81*(13), 2289–2303. https://doi.org/10.1029/JA081i013p02289

McKean, M. E., Omidi, N., & Krauss-Varban, D. (1996). Magnetosheath dynamics downstream of low mach number shocks. *Journal of Geophysical Research*, *101*(A9), 20,013–20,022. https://doi.org/10.1029/96JA01461

Merkin, V. G., & Lyon, J. G. (2010). Effects of the low-latitude ionospheric boundary condition on the global magnetosphere. *Journal of Geophysical Research*, *115*, A10202. https://doi.org/10.1029/2010JA015461

Merkin, V. G., Lyon, J. G., & Claudepierre, S. G. (2013). Kelvin-Helmholtz instability of the magnetospheric boundary in a three-dimensional global MHD simulation during northward IMF conditions. *Journal of Geophysical Research: Space Physics*, *118*, 5478–5496. https://doi.org/10.1002/jgra.50520

Newell, P. T., Sotirelis, T., Liou, K., & Rich, F. J. (2008). Pairs of solar wind-magnetosphere coupling functions: Combining a merging term with a viscous term works best. *Journal of Geophysical Research*, *113*, A04218. https://doi.org/10.1029/2007JA012825

Rout, D., Chakrabarty, D., Sekar, R., Reeves, G. D., Ruohoniemi, J. M., Pant, T. K., & Shiokawa, K. (2016). An evidence for prompt electric field disturbance driven by changes in the solar wind density under northward IMF Bz condition. *Journal of Geophysical Research: Space Physics*, *121*, 4800–4810. https://doi.org/10.1002/2016JA022475

Ruohoniemi, J. M., & Greenwald, R. A. (1996). Statistical patterns of high-latitude convection obtained from goose bay HF radar observations. *Journal of Geophysical Research*, *101*(A10), 21,743–21,763. https://doi.org/10.1029/96JA01584

Siscoe, G. L., Crooker, N. U., & Siebert, K. D. (2002). Transpolar potential saturation: Roles of Region 1 current system and solar wind ram pressure. *Journal of Geophysical Research*, *107*(A10), 1321. https://doi.org/10.1029/2001JA009176

Weimer, D. R. (2005). Improved ionospheric electrodynamic models and application to calculating joule heating rates. *Journal of Geophysical Research*, *110*, A05306. https://doi.org/10.1029/2004JA010884

Zhang, B., Brambles, O. J., Cassak, P. A., Ouellette, J. E., Wiltberger, M., Lotko, W., & Lyon, J. G. (2017). Transition from global to local control of dayside reconnection from ionospheric-sourced mass loading. *Journal of Geophysical Research: Space Physics*, *122*, 9474–9488. https://doi.org/10.1002/2016JA023646